Subspace-Rytov Approximation Inversion Method for Inverse Scattering Problems

Tiantian Yin®, Li Pan, *Member, IEEE*, and Xudong Chen®, *Fellow, IEEE*

Abstract— In this article, we propose a novel non-iterative method, viz., the subspace-Rytov approximation (SRA) method, to solve inverse scattering problems. This method improves the inversion results of the Rytov approximation (RA) by retaining the integral term neglected therein. The evaluation of this integral involves two approximations. The integrand is approximated with its major part that results from the major induced current and is calculated by the subspace method. The integration on the whole space is approximated by an integration on a finite domain by truncation. Tests with both synthetic data and measured data show that the SRA method outperforms the RA inversion method and the Born approximation (BA) inversion method, and that the SRA outperforms the modified BA (MBA) method in accuracy for relatively large scatterers.

Index Terms— Inverse scattering, non-iterative method, Rytov approximation (RA), subspace method.

I. INTRODUCTION

AN INVERSE scattering technique reconstructs the spatial distribution of some physical properties by inverting the measured scattering data. It has found extensive applications in a variety of areas, such as nondestructive evaluation, medical imaging, geophysics, remote sensing, and security checks [1]. The exact model of inverse scattering is nonlinear, and therefore, the inverse scattering problem is usually cast into a nonlinear optimization problem, which we must solve by iterative methods [2]–[6]. Under certain conditions, the nonlinear model can be simplified as an approximate linear model, which can be solved by non-iterative methods at lower computational cost.

Over the past decades, a number of non-iterative inversion methods [7]–[13] have been proposed based on different types of approximation, among which the Born approximation (BA) method and the Rytov approximation (RA) method are most widely used. Their validity has been studied in depth in many publications [7], [14]. It was found that the first-order RA can yield better results for electrically large scatterers with low contrasts compared with the first-order BA. Both

BA and RA could be enhanced by retaining and approximating the neglected term [8], [15]. These two inversion methods have also been combined to solve microwave near-field imaging problems [16]. RA has also been applied in the iterative method [17] and further incorporated with interval analysis [18] and Bayesian compressive sensing [19]. The distorted Rytov iterative method (DRIM) has been proposed for inversion of phaseless data [20].

The article proposes a non-iterative RA-based inversion method, referred to as the subspace-RA (SRA), to solve inverse scattering problems. The SRA is able to reconstruct scatterers with higher contrast than the RA and, as a non-iterative method, has much lower computational cost than the DRIM. These advantages made the SRA a good candidate for the inverse scattering applications involving not only fast imaging but also high contrast scatterers for which the RA fails. As we know, the RA method is applicable only for weak scatterers, because it neglects a term, which is an integral transform over infinite domain. In the SRA method, this term is retained to acquire enhanced inversion results. Nevertheless, to evaluate this term, is numerically challenging for two reasons: 1) the integral is over an infinite domain and 2) it is difficult to evaluate the integrand before solving the inverse problem. To tackle the first difficulty, we introduce the concept of truncated integral domain (TID) and prove that the neglected integral transform over infinite domain can be well approximated by an integral over a TID. To address the second problem, we adopt the subspace method to find the major induced current, which is then used to produce an approximate evaluation of the integrand. Both analytical and numerical analyses of the approximation errors are provided as a guideline to strike the balance between accuracy and computational cost. Tests with both synthetic and experimental data show that the SRA outperforms the RA and BA methods, and that the SRA outperforms the modified BA (MBA) method in case of relatively large scatterers. In addition, the SRA method can be combined with the MBA method, to produce a joint method as an alternative approach to inverse scattering problems.

We highlight that the application of subspace to RA is different from and more difficult than all previously reported subspace methods in the field of inverse scattering, such as in [5], [13], and [21]. The subspace methods employed in all previous publications involve a finite computation domain, which is referred to the domain of interests (DOI). In comparison, the subspace method involved in the SRA deals with an infinite integral domain, which needs a careful numerical truncation. On the other hand, the SRA shares the salient feature of the

Tiantian Yin and Xudong Chen are with the Department of Electrical and Computer Engineering, National University of Singapore, Singapore 117583 (e-mail: e0021489@u.nus.edu; elechenx@nus.edu.sg).

Li Pan is with the Huawei Singapore Research Centre, Singapore 138588 (e-mail: mr.panli@gmail.com).

previously reported subspace methods; i.e., only a thin singular value decomposition (SVD) of the mapping matrix is required, and consequently, the computational cost is relatively low. In addition, no iterations are required for the calculation of the major induced current.

The structure of this article is as follows. In Section II, the formulations of both the forward problem and the inverse problem are provided. This section also provides the formulations quantifying the contribution of the neglected term in RA and the errors due to the two approximations made in SRA. In Section III, the simulation results of the contribution of the neglected term in RA and the errors due to the two approximations are provided. The inversion results using different methods are given and compared. In Section IV, the conclusions and discussions are provided.

In this article, $\|\cdot\|_F$ and $\|\cdot\|$ denote the Frobenius norm and the Euclidean norm, respectively. The superscript H represents the Hermitian operator, and the superscript T represents the transpose operator. The time convention of $e^{-i\omega t}$ is adopted and suppressed.

II. FORMULATIONS

A. Forward Problem

We consider a 2-D transverse magnetic (TM) configuration, as shown in Fig. 1. The whole space is homogeneous except for some scatterers. All scatterers are located within the DOI that is also denoted as D, which is illuminated by incident waves from an array of transmitting antennas located in the region T that is outside of the DOI. The scattered wave is measured by an array of receiving antennas that are located in the region S that is outside of the DOI. In forward modeling, the scattered field is represented as a function of the spatial distribution of permittivity, given the incident waves. The scattered electric field within D is given as

$$E_s(\boldsymbol{r}) = i\omega\mu_0 \int\int_D g(\boldsymbol{r},\boldsymbol{r}')J(\boldsymbol{r}')d\boldsymbol{r}' = E_t(\boldsymbol{r}) - E_{\text{inc}}(\boldsymbol{r}) \quad (1)$$

where ω is the angular frequency of the incidence, μ_0 is the permeability of the free space, E_t is the total electric field, and E_{inc} is the incident electric field, $\boldsymbol{r}, \boldsymbol{r}' \in D$. The induced current is defined as

$$J(\boldsymbol{r}') = \chi(\boldsymbol{r}') \cdot E_t(\boldsymbol{r}') \quad (2)$$

where $\chi(\boldsymbol{r}') = -i\omega\varepsilon_0[\varepsilon_r(\boldsymbol{r}') - 1]$ is the normalized contrast. The Green's function is

$$g(\boldsymbol{r},\boldsymbol{r}') = \frac{i}{4}H_0^{(1)}(k|\boldsymbol{r} - \boldsymbol{r}'|). \quad (3)$$

Discretization of (1) via the method of moments as in [1] yields

$$\overline{\overline{G}}_d \cdot \bar{J} = \overline{E}_t - \overline{E}_{\text{inc}} \quad (4)$$

where $\bar{J}$, $\overline{E}_t$, $\overline{E}_{\text{inc}}$ are vectors of length M_{DOI}, and M_{DOI} is the number of cells in DOI. $\overline{\overline{G}}_d$ is defined as

$$\overline{\overline{G}}_d(m, m')$$
$$= \begin{cases} \dfrac{-\eta\pi a}{2} J_1(k_0 a) H_0^{(1)}\left[k_0\overline{\overline{R}}(m, m')\right], & \text{if } m \neq m' \\ \dfrac{-\eta\pi a}{2} H_1^{(1)}(k_0 a) - \dfrac{i\eta}{k_0}, & \text{if } m = m' \end{cases} \quad (5)$$
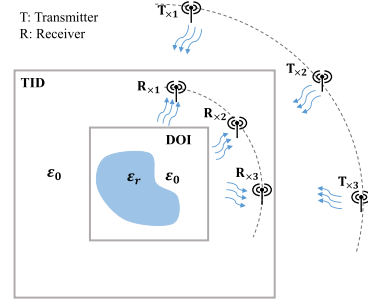

Fig. 1. DOI and TID.

where $m, m' = 1, 2, \ldots, M_{\text{DOI}}$, and η, k_0 are the impedance and wavenumber of free space, respectively, a is the radius of the circle that has the same area as the square cells, and $\overline{\overline{R}}(m, m')$ is the distance between the centers of the mth and the m'th cells in the DOI.

The scattered field received by a receiving antenna is

$$E_s(\boldsymbol{r}) = i\omega\mu_0 \int\int_D g(\boldsymbol{r},\boldsymbol{r}')J(\boldsymbol{r}')d\boldsymbol{r}' \quad (6)$$

where $\boldsymbol{r} \in S, \boldsymbol{r}' \in D$. Discretization of (6) gives

$$\overline{E}_s = \overline{\overline{G}}_s \cdot \bar{J} \quad (7)$$

where $\bar{E}_s$ is a vector of length N_s, and N_s is the number of receiving antennas

$$\overline{\overline{G}}_s(n, m) = \frac{-\eta\pi a}{2} J_1(k_0 a) H_0^{(1)}\left[k_0\overline{\overline{R}}(n, m)\right] \quad (8)$$

and $m = 1, 2, \ldots, M_{\text{DOI}}$, $n = 1, 2, \ldots, N_s$. $\overline{\overline{R}}(n, m)$ is the distance between the center of the mth cell in the DOI and the nth receiving antenna.

B. Principle of SRA: Two Approximations

It is shown in [7] that the scattering phenomenon can also be exactly reformulated as in

$$E_{\text{inc}}(\boldsymbol{r})\psi(\boldsymbol{r}) = \int_{-\infty}^{\infty}\int_{-\infty}^{\infty} g(\boldsymbol{r},\boldsymbol{r}')\left[\nabla'\psi(\boldsymbol{r}')\right]^2 E_{\text{inc}}(\boldsymbol{r}')d\boldsymbol{r}'$$
$$+ \int\int_D g(\boldsymbol{r},\boldsymbol{r}')i\omega\mu_0\chi(\boldsymbol{r}')E_{\text{inc}}(\boldsymbol{r}')d\boldsymbol{r}' \quad (9)$$

where

$$\psi(\boldsymbol{r}') = \ln\left[\frac{E_t(\boldsymbol{r}')}{E_{\text{inc}}(\boldsymbol{r}')}\right] \quad (10)$$

and

$$\left[\nabla'\psi(\boldsymbol{r}')\right]^2 = \left[\nabla'\psi(\boldsymbol{r}')\right] \cdot \left[\nabla'\psi(\boldsymbol{r}')\right]$$
$$= \frac{1}{[E_{\text{inc}}(\boldsymbol{r}')E_t(\boldsymbol{r}')]^2}$$
$$\times \left\{ \begin{bmatrix} \left[\dfrac{\partial E_s(\boldsymbol{r}')}{\partial x'}E_{\text{inc}}(\boldsymbol{r}') - \dfrac{\partial E_{\text{inc}}(\boldsymbol{r}')}{\partial x'}E_s(\boldsymbol{r}')\right]^2 \\ + \left[\dfrac{\partial E_s(\boldsymbol{r}')}{\partial y'}E_{\text{inc}}(\boldsymbol{r}') - \dfrac{\partial E_{\text{inc}}(\boldsymbol{r}')}{\partial y'}E_s(\boldsymbol{r}')\right]^2 \end{bmatrix} \right\}. \quad (11)$$

There are two integral terms on the right-hand side of (9). In RA [9], the first integral is neglected, that is,

$$E_{\text{inc}}(\boldsymbol{r})\psi(\boldsymbol{r}) \approx \int\!\!\int_D g(\boldsymbol{r},\boldsymbol{r}')i\omega\mu_0\chi(\boldsymbol{r}')E_{\text{inc}}(\boldsymbol{r}')d\boldsymbol{r}'. \quad (12)$$

As discussed in many publications [7], [9], for the case of weak scatterers with small electrical dimensions, where we have $(\nabla'\psi)^2 \ll i\omega\mu_0\chi$, the neglection in RA is valid. Otherwise, noticeable error results from neglecting the first integral in (9).

If we retain the term neglected in RA, the inversion result can be improved naturally. Unfortunately, it is challenging to evaluate this integral term for two reasons. First, dissimilar to that of the second integral, the integral domain for the first integral is the whole space instead of only DOI, as suggested by (11). Second, it is difficult to find ψ in the integrand before solving the inverse scattering problem.

In the proposed SRA method, the first integral in (9) is retained, and the two challenges are resolved using two approximations. In the first approximation, we perform the integral on a finite TID instead of the whole space. In the second approximation, we use a subspace method to evaluate the major part of ψ in the TID that results from the major induced current. The two approximations used in the SRA method are summarized as

$$\int\!\!\int_D g(\boldsymbol{r},\boldsymbol{r}')i\omega\mu_0\chi(\boldsymbol{r}')E_{\text{inc}}(\boldsymbol{r}')d\boldsymbol{r}'$$
$$= E_{\text{inc}}(\boldsymbol{r})\psi(\boldsymbol{r}) - \int_{-\infty}^{\infty}\!\!\int_{-\infty}^{\infty} g(\boldsymbol{r},\boldsymbol{r}')[\nabla'\psi(\boldsymbol{r}')]^2 E_{\text{inc}}(\boldsymbol{r}')d\boldsymbol{r}'$$
$$\approx E_{\text{inc}}(\boldsymbol{r})\psi(\boldsymbol{r}) - \int\!\!\int_{TID} g(\boldsymbol{r},\boldsymbol{r}')[\nabla'\psi(\boldsymbol{r}')]^2 E_{\text{inc}}(\boldsymbol{r}')d\boldsymbol{r}'$$
$$\approx E_{\text{inc}}(\boldsymbol{r})\psi(\boldsymbol{r}) - \int\!\!\int_{TID} g(\boldsymbol{r},\boldsymbol{r}')[\nabla'\psi^+(\boldsymbol{r}')]^2 E_{\text{inc}}(\boldsymbol{r}')d\boldsymbol{r}'$$
$$(13)$$

where ψ^+ is the major part of ψ evaluated in the TID, and the evaluation of $[\nabla'\psi^+(\boldsymbol{r}')]^2$ in the TID will be discussed in Section II-E. The value of ψ evaluated at the receivers is calculated using the total field and the incident field provided by the measurement data.

C. Validity Analysis of Using TID for the First Integral in (9)

To check whether it is valid to truncate the infinite integral domain of the first integral in (9) into TID, it is of great interest to evaluate the value of the integral of the first integrand in (9) over the complement of TID. Therefore, we rewrite the first integral in (9) in a polar coordinate system as

$$T(\rho,\phi) = \int_0^{\infty}\!\!\int_0^{2\pi} g(\rho,\phi,\rho',\phi')[\nabla'\psi(\rho',\phi')]^2$$
$$\times E_{\text{inc}}(\rho',\phi')\rho'd\phi'd\rho'$$
$$= \int_0^r F(\rho,\phi,\rho')d\rho' + \int_r^{\infty} F(\rho,\phi,\rho')d\rho' \quad (14)$$

where the first and second terms are the integrals over a circular TID and its complement, respectively. The function

$F(\rho,\phi,\rho')$ is defined as

$$F(\rho,\phi,\rho') = \int_0^{2\pi} g(\rho,\phi,\rho',\phi')[\nabla'\psi(\rho',\phi')]^2$$
$$\times E_{\text{inc}}(\rho',\phi')\rho'd\phi'. \quad (15)$$

We will evaluate $F(\rho,\phi,\rho')$ both analytically and numerically for the case of an incident plane wave with an incidence angle of $0°$ with respect to the x-axis, that is,

$$E_{\text{inc}}(\rho',\phi') = e^{ik_0\rho'\cos\phi'}. \quad (16)$$

For an arbitrary scatterer, the scattered field can be represented by [22]

$$E_s(\rho',\phi') = -\frac{\omega\mu_0}{4}\sum_n b_n H_n^{(1)}(k\rho')e^{in\phi'}. \quad (17)$$

The derivation in the appendix produces an analytical formula of $F(\rho,\phi,\rho')$ for large ρ' as

$$F_{\text{anal}}(\rho,\phi,\rho') = \frac{\exp(i4k\rho')}{4\pi\rho'}i\omega^2\mu_0^2$$
$$\times \exp(ik\rho\cos\phi)\sum_p\sum_q b_pb_qi^{p+q}. \quad (18)$$

Substitution of (18) into the second term in (14) yields $[(i\omega^2\mu_0^2/4\pi)\exp(ik\rho\cos\phi)\sum_p\sum_q b_pb_qi^{p+q}] \times [-i \times \text{si}(4kr) - \text{Ci}(4kr)]$, where $\text{si}(4kr) = -\int_{4kr}^{\infty}(\sin(t)/t)dt$, $\text{Ci}(4kr) = -\int_{4kr}^{\infty}(\cos(t)/t)dt$. Since $\text{si}(4kr)$ and $\text{Ci}(4kr)$ both asymptotically approach zero when r approaches infinity [23], the second term in (14) is negligible if r is large enough. Therefore, it is valid to truncate the infinite integral domain of the first integral in (9) into TID.

For further verification of F_{anal}, the numerical formula of $F(\rho,\phi,\rho')$ is also derived. We discretize the circle of radius ρ' into N_c elements and denote the polar coordinate of the center of the nth element as $(\rho',\bar{\phi}'(n))$. Then, we obtain the numerical formula of $F(\rho,\phi,\rho')$

$$F_{\text{num}} = \overline{G}_{\text{R–C}}^T \cdot \overline{\overline{P}}_{1,\text{C}} \cdot \overline{E}_{\text{inc,C}} \quad (19)$$

where the subscript C denotes quantities evaluated at the circle. $\bar{G}_{\text{R–C}}$, which is a vector with N_c elements, is defined as

$$\overline{G}_{\text{R–C}}(n) = \frac{i}{4}\frac{2\pi\rho'}{N_c}H_0^{(1)}[k_0\overline{R}_{\text{R–C}}(n)] \quad (20)$$

where $\bar{R}_{\text{R–C}}(n) = \sqrt{\rho^2 + \rho'^2 - 2\rho\rho'\cos(\phi - \bar{\phi}'(n))}$. (ρ,ϕ) is the polar coordinate of the observation point, $n = 1, 2, \ldots, N_\text{C}$. $\bar{E}_{\text{inc,C}}$ is of length N_c and defined as

$$\bar{E}_{\text{inc,C}}(n) = \exp[ik_0\rho'\cos\overline{\phi}'(n)]. \quad (21)$$

$\overline{\overline{P}}_{1,\text{C}}$ is a diagonal matrix with the diagonal elements being evaluations of $(\nabla'\psi)^2$ in (11) that are explicitly given in Table I. $\bar{G}_{\text{x,C–DOI}}^n$, $\bar{G}_{\text{y,C–DOI}}^n$, and $\overline{\overline{R}}_{\text{C–DOI}}$ used in the formula of $\overline{\overline{P}}_{1,\text{C}}$ are also defined in Table I. In the definitions of the matrices, the quantities without the subscript C, including $\bar{J}$, $\bar{x}$, and $\bar{y}$, are evaluated in the DOI. $\bar{G}_{\text{x,C–DOI}}^n$, $\bar{G}_{\text{y,C–DOI}}^n$, $\bar{J}$, $\bar{x}$, and $\bar{y}$ are vectors of length M_{DOI}, $\bar{E}_{\text{s,C}}$, $\bar{E}_{\text{t,C}}$, $\bar{x}_\text{C}$, and $\bar{y}_\text{C}$ are vectors of length N_C. $\overline{\overline{R}}_{\text{C–DOI}}$ is of size $N_\text{c} \times M_{\text{DOI}}$.

TABLE I
DISCRETIZATION OF $(\nabla' \psi_1)^2$ IN SECTIONS II-C AND II-D

Section II C $n = 1, 2, \ldots, N_C, m = 1, 2, \ldots, M_{DOI}$	Section II D $m = 1, 2, \ldots, M_{TID}, m' = 1, 2, \ldots, M_{TID}$
$\overline{\overline{P}}_{1,C}(n,n) = \dfrac{1}{\left[\bar{E}_{t,C}(n) \cdot \bar{E}_{inc,C}(n)\right]^2}$ $\times \left\{ \begin{array}{l} \left[\overline{G}_{x,C\text{-DOI}}^{n}{}^T \cdot \bar{J} \cdot \bar{E}_{inc,C}(n) - ik_0 \bar{E}_{inc,C}(n) \cdot \bar{E}_{s,C}(n)\right]^2 + \\ \left[\overline{G}_{y,C\text{-DOI}}^{n}{}^T \cdot \bar{J} \cdot \bar{E}_{inc,C}(n)\right]^2 \end{array} \right\}$	$\overline{\overline{P}}_{1,TID}(m,m) = \dfrac{1}{\left[\bar{E}_{t,TID}(m) \cdot \bar{E}_{inc,TID}(m)\right]^2}$ $\times \left\{ \begin{array}{l} \left[\overline{G}_{x,TID}^{m}{}^T \cdot \bar{J}_{TID} \cdot \bar{E}_{inc,TID}(m) - ik_0 \cos\theta_{inc} \bar{E}_{inc,TID}(m) \cdot \bar{E}_{s,TID}(m)\right]^2 + \\ \left[\overline{G}_{y,TID}^{m}{}^T \cdot \bar{J}_{TID} \cdot \bar{E}_{inc,TID}(m) - ik_0 \sin\theta_{inc} \bar{E}_{inc,TID}(m) \cdot \bar{E}_{s,TID}(m)\right]^2 \end{array} \right\}$
$\overline{G}_{x,C\text{-DOI}}^{n}(m) =$ $\dfrac{k_0 \eta \pi a}{2} J_1(k_0 a) H_1^{(1)}\left[k_0 \overline{\overline{R}}_{C\text{-DOI}}(n,m)\right] \dfrac{\bar{x}_C(n) - \bar{x}(m)}{\overline{\overline{R}}_{C\text{-DOI}}(n,m)}$	$\overline{G}_{x,TID}^{m}(m') =$ $\begin{cases} \dfrac{k_0 \eta \pi a}{2} J_1(k_0 a) H_1^{(1)}\left[k_0 \overline{\overline{R}}_{TID}(m,m')\right] \dfrac{\bar{x}_{TID}(m) - \bar{x}_{TID}(m')}{\overline{\overline{R}}_{TID}(m,m')}, & \text{if } m \neq m' \\ 0, & \text{if } m = m' \end{cases}$
$\overline{G}_{y,C\text{-DOI}}^{n}(m) =$ $\dfrac{k_0 \eta \pi a}{2} J_1(k_0 a) H_1^{(1)}\left[k_0 \overline{\overline{R}}_{C\text{-DOI}}(n,m)\right] \dfrac{\bar{y}_C(n) - \bar{y}(m)}{\overline{\overline{R}}_{C\text{-DOI}}(n,m)}$	$\overline{G}_{y,TID}^{m}(m') =$ $\begin{cases} \dfrac{k_0 \eta \pi a}{2} J_1(k_0 a) H_1^{(1)}\left[k_0 \overline{\overline{R}}_{TID}(m,m')\right] \dfrac{\bar{y}_{TID}(m) - \bar{y}_{TID}(m')}{\overline{\overline{R}}_{TID}(m,m')}, & \text{if } m \neq m' \\ 0, & \text{if } m = m' \end{cases}$
$\overline{\overline{R}}_{C\text{-DOI}}(n,m) = \sqrt{\left[\bar{x}_C(n) - \bar{x}(m)\right]^2 + \left[\bar{y}_C(n) - \bar{y}(m)\right]^2}$	$\overline{\overline{R}}_{TID}(m,m') = \sqrt{\left[\bar{x}_{TID}(m) - \bar{x}_{TID}(m')\right]^2 + \left[\bar{y}_{TID}(m) - \bar{y}_{TID}(m')\right]^2}$

D. First Approximation and Its Error

To strike a balance between accuracy and computational cost, it is worthwhile to quantify the error due to the first approximation, which is the truncation of the integral domain of the first integral in (9), as a function of the size of the TID.

In this section, it is assumed that a scatterer is illuminated by an incident plane wave with the incident angle of θ_{inc}. Using the TID with M_{TID} pixels and the DOI with M_{DOI} pixels as the integral domains for the first and the second integral in the discretized version of (9), respectively, we obtain

$$\bar{\bar{E}}_{inc,R} \cdot \bar{\psi}_R - \frac{1}{i\omega\mu_0} \overline{\overline{G}}_{R-TID} \cdot \overline{\overline{P}}_{1,TID} \cdot \overline{E}_{inc,TID} \approx \overline{\overline{G}}_s \cdot \overline{\overline{E}}_{inc} \cdot \bar{\chi} \tag{22}$$

where the subscript TID denotes quantities evaluated in the TID. The subscript R denotes quantities evaluated at the receiver. $\bar{E}_{inc,TID}$ is a vector of length M_{TID}. $\overline{\overline{E}}_{inc,R}$ and $\overline{\overline{E}}_{inc}$ are diagonal matrices with diagonal elements being incident fields, which are of sizes $N_s \times N_s$ and $M_{DOI} \times M_{DOI}$, respectively. $\bar{\psi}_R$ is of length N_s. $\overline{\overline{G}}_{R-TID}$, which is of size $N_s \times M_{TID}$, is defined as

$$\overline{\overline{G}}_{R-TID}(n,m) = \begin{cases} \dfrac{-\eta\pi a}{2} J_1(k_0 a) H_0^{(1)}\left(k_0 \overline{\overline{R}}_{R-TID}(n,m)\right), \\ \qquad \text{if } \overline{\overline{R}}_{R-TID}(n,m) > a \\ \dfrac{-\eta\pi a}{2} H_1^{(1)}(k_0 a) - \dfrac{i\eta}{k_0}, \\ \qquad \text{if } \overline{\overline{R}}_{R-TID}(n,m) \leq a \end{cases} \tag{23}$$

where $n = 1, 2, \ldots, N_s$ and $m = 1, 2, \ldots, M_{TID}$. $\overline{\overline{R}}_{R-TID}$ is of size $N_s \times M_{TID}$. Note that $\overline{\overline{G}}_{R-TID}$ is different from $\overline{\overline{G}}_s$ in two aspects. First, they are of different sizes. $\overline{\overline{G}}_{R-TID}$ is of size $N_s \times M_{TID}$, and $\overline{\overline{G}}_s$ is of size $N_s \times M_{DOI}$. Second, the definition of the elements in $\overline{\overline{G}}_{R-TID}$ is different when the distances between the corresponding receivers and the corresponding centers of the cells in the TID are smaller than or equal to a. Note that the receivers, which are always outside the DOI, could be within the TID, as shown in Fig. 1. $\overline{\overline{P}}_{1,TID}$ in (22) is defined in Table I. $\bar{G}_{x,TID}^{m}$, $\bar{G}_{y,TID}^{m}$, and $\overline{\overline{R}}_{TID}$ used in the formula of $\overline{\overline{P}}_{1,TID}$ are also defined in Table I. $\bar{J}_{TID}$ is obtained by padding zeros to $\bar{J}$, and it is of length M_{TID}. $\bar{E}_{s,TID}$, $\bar{E}_{t,TID}$, $\bar{G}_{x,TID}^{m}$, and $\bar{G}_{y,TID}^{m}$ are all vectors of length M_{TID}.

Using the TID for the first integral of (9) in the discretization will result in differences between the values obtained from two sides of (22). To quantify the errors introduced using TIDs with different sizes, the right-hand side of (22) is defined as the accurate value

$$\overline{R}_{acc} = \overline{\overline{G}}_s \cdot \overline{\overline{E}}_{inc} \cdot \bar{\chi} \tag{24}$$

and the left-hand side of (22) is defined as

$$\overline{R}_{trunc} = \bar{\bar{E}}_{inc,R} \cdot \bar{\psi}_R - \frac{1}{i\omega\mu_0} \overline{\overline{G}}_{R-TID} \cdot \overline{\overline{P}}_{1,TID} \cdot \overline{E}_{inc,TID}. \tag{25}$$

The error of due to the first approximation (truncation) is defined as

$$err_1 = \frac{\left\| \overline{R}_{trunc} - \overline{R}_{acc} \right\|}{\left\| \overline{R}_{acc} \right\|}. \tag{26}$$

Note that, after discretization, the derivatives in (11) are calculated analytically in the definition of $\overline{\overline{P}}_{1,\mathrm{TID}}$ instead of using the numerical difference method. There are mainly two advantages of the analytical calculations over the numerical difference method. First, the calculation of logarithm of complex number in the first integral of (9) is avoided in the analytical calculations, and there is no more phase-wrapping problem that is due to the complex-valued logarithmic function in the first integral of (9). Note that the use of (11) avoids the phase-wrapping problem only on the right-hand side of (9) but not in the evaluation of ψ on the left-hand side of (9). Second, the computation cost using the analytical calculations of the derivatives is $O(M_{\mathrm{TID}}\log M_{\mathrm{TID}})$ by employing the fast Fourier transform (FFT)-accelerated algorithm [1]. In comparison, the computational cost of the numerical difference method is $O(M_{\mathrm{TID}}^2)$.

E. Second Approximation and Error Due to Both Approximations

In the inverse problem, the major induced current can be calculated deterministically using the subspace method. As has been mentioned before, the major induced current helps to improve the approximation of the total electric field in non-iterative inversion methods. It is of our interests to see how the integral domain truncation errors will vary when ψ in the first integral of (9) is calculated by approximating the total field by replacing induced current with its major part.

In the subspace method, after SVD of $\overline{\overline{G}}_{\mathrm{s}} = \bar{\bar{U}} \cdot \bar{\bar{\Sigma}} \cdot \bar{\bar{V}}^H$, the induced current could be represented as a linear combination of the right singular vectors, i.e., $\bar{J} = \overline{\overline{V}} \cdot \bar{\alpha}$. As we know from [5], the induced current can be divided into two complementary and orthogonal parts, that is, the major and minor induced currents, $\bar{J} = \bar{J}^+ + \bar{J}^-$. The major induced current and the minor induced current are represented as $\bar{J}^+ = \overline{\overline{V}}^+ \cdot \bar{\alpha}^+$ and $\bar{J}^- = \overline{\overline{V}}^- \cdot \bar{\alpha}^-$, respectively. $\overline{\overline{V}}^+$ and $\overline{\overline{V}}^-$ are composed of the first L and the remaining columns of $\overline{\overline{V}}$, respectively. $\bar{\alpha}^+$ and $\bar{\alpha}^-$ are composed of the first L and the remaining current coefficients in $\bar{\alpha}$, respectively. Note that, in the implementation, since we are only interested in the first L singular vectors in $\bar{\bar{U}}$ and $\overline{\overline{V}}$, only thin SVD of $\overline{\overline{G}}_{\mathrm{s}}$ is needed, and the computational cost is $O(M_{\mathrm{DOI}}N_{\mathrm{s}}^2)$ [1].

To obtain the major induced current $\bar{J}^+$ in the DOI, the major induced current coefficients are calculated as in [5]

$$\alpha_j = \frac{\overline{u}_j^H \cdot \bar{E}_{\mathrm{s}}}{\sigma_j} \tag{27}$$

where $\bar{u}_j$ is the jth left singular vector of $\overline{\overline{G}}_{\mathrm{s}}$, and σ_j is the jth singular value, $j = 1, 2, \ldots, L$. The value of L could be determined using the discrepancy principle [24]. After the major induced current $\bar{J}^+$ in the DOI is calculated, within the TID, the approximated total electric field is represented by a vector of length M_{TID}

$$\overline{E}_{\mathrm{ta,TID}} = \overline{E}_{\mathrm{inc,TID}} + \overline{\overline{G}}_{\mathrm{d,TID}} \cdot \bar{J}_{\mathrm{TID}}^+ \tag{28}$$

where $\bar{J}_{\mathrm{TID}}^+$, which is of length M_{TID}, is obtained by padding zeros to $\bar{J}^+$. $\overline{\overline{G}}_{\mathrm{d,TID}}$ is the radiation operator within the TID,

which is defined similarly as $\overline{\overline{G}}_{\mathrm{d}}$ in (5). Here, we define the discretization matrix of $[\nabla'\Psi^+(\boldsymbol{r}'))]^2$ in (13) as $\overline{\overline{P}}_{2,\mathrm{TID}}$. By replacing $\overline{\overline{P}}_{1,\mathrm{TID}}$ in (25) with $\overline{\overline{P}}_{2,\mathrm{TID}}$, it is defined that

$$\overline{R}_{\mathrm{trunc}}^+ = \overline{\overline{E}}_{\mathrm{inc,R}} \cdot \bar{\psi}_{\mathrm{R}} - \frac{1}{i\omega\mu_0}\overline{\overline{G}}_{\mathrm{R-TID}} \cdot \overline{\overline{P}}_{2,\mathrm{TID}} \cdot \overline{E}_{\mathrm{inc,TID}} \tag{29}$$

where $\overline{\overline{P}}_{2,\mathrm{TID}}$ is an $M_{\mathrm{TID}} \times M_{\mathrm{TID}}$ diagonal matrix, of which the mth diagonal element is given by

$$\begin{aligned}\overline{\overline{P}}_{2,\mathrm{TID}}&(m,m)\\[4pt]&= \frac{1}{\left[\bar{E}_{\mathrm{ta,TID}}(m) \cdot \bar{E}_{\mathrm{inc,TID}}(m)\right]^2}\\[4pt]&\times\left\{\begin{array}{l}\left[\overline{G}_{\mathrm{x,TID}}^{mT} \cdot \overline{J}_{\mathrm{TID}}^+ \cdot \bar{E}_{\mathrm{inc,TID}}(m)\right.\\ \left.-ik_0\cos\theta_{\mathrm{inc}}\bar{E}_{\mathrm{inc,TID}}(m) \cdot \bar{E}_{\mathrm{sa,TID}}(m)\right]^2\\ +\left[\overline{G}_{\mathrm{y,TID}}^{m\,T} \cdot \overline{J}_{\mathrm{TID}}^+ \cdot \bar{E}_{\mathrm{inc,TID}}(m)\right.\\ \left.-ik_0\sin\theta_{\mathrm{inc}}\bar{E}_{\mathrm{inc,TID}}(m) \cdot \bar{E}_{\mathrm{sa,TID}}(m)\right]^2\end{array}\right\}\end{aligned} \tag{30}$$

where $m = 1, 2, \ldots, M_{\mathrm{TID}}$ and $\bar{E}_{\mathrm{sa,TID}} = \overline{\overline{G}}_{\mathrm{d,TID}} \cdot \bar{J}_{\mathrm{TID}}^+$. The error due to both the first and second approximations is defined as

$$err_{1,2} = \frac{\left\|\overline{R}_{\mathrm{trunc}}^+ - \overline{R}_{\mathrm{acc}}\right\|}{\left\|\overline{R}_{\mathrm{acc}}\right\|}. \tag{31}$$

It is obvious that the truncation error defined in (31) is expected to be larger than the truncation error defined in (26) due to the replacement of ψ by ψ^+.

F. Inverse Problem

1) RA Inversion Method: After discretization, the RA in (12) becomes

$$\overline{\overline{G}}_{\mathrm{s}} \cdot \overline{\overline{E}}_{\mathrm{inc}} \cdot \bar{\chi} \approx \overline{\overline{E}}_{\mathrm{inc,R}} \cdot \overline{\psi}_{\mathrm{R}}. \tag{32}$$

Hence, the cost function of the RA inversion method is defined as

$$f(\overline{\chi}) = \sum_{p=1}^{N_{\mathrm{i}}}\left\|\overline{\overline{G}}_{\mathrm{s}} \cdot \overline{\overline{E}}_{\mathrm{inc}}^p \cdot \bar{\chi} - \overline{\overline{E}}_{\mathrm{inc,R}}^p \cdot \overline{\psi}_{\mathrm{R}}^p\right\|^2 + \beta\|\overline{\chi}\|^2 \tag{33}$$

where p is the index of incidences, and N_{i} is the number of incidences. The L-curve method [25], which is implemented using a MATLAB package [26], is used to determine the coefficient β of the Tikhonov regularization [1]. The minimizer of (33) is

$$\begin{aligned}\overline{\chi} = \Bigg[&\sum_{p=1}^{N_{\mathrm{i}}}\left(\overline{\overline{G}}_{\mathrm{s}} \cdot \overline{\overline{E}}_{\mathrm{inc}}^p\right)^H \cdot \left(\overline{\overline{G}}_{\mathrm{s}} \cdot \overline{\overline{E}}_{\mathrm{inc}}^p\right) + \beta\overline{\overline{I}}\Bigg]^{-1}\\[4pt]&\cdot\left[\sum_{p=1}^{N_{\mathrm{i}}}\left(\overline{\overline{G}}_{\mathrm{s}} \cdot \overline{\overline{E}}_{\mathrm{inc}}^p\right)^H \cdot \overline{\overline{E}}_{\mathrm{inc,R}}^p \cdot \overline{\psi}_{\mathrm{R}}^p\right]. \tag{34}\end{aligned}$$

2) SRA Inversion Method: In the SRA method, as mentioned in Section II-B, the neglected term in RA is retained and approximated by replacing ψ with its major part and using a TID as the integral domain. By substituting $\overline{\overline{P}}_{2,\text{TID}}$ of (30) into $\overline{\overline{P}}_{1,\text{TID}}$ of (22), the approximations in the SRA method are summarized as

$$\bar{\bar{E}}_{\text{inc,R}} \cdot \bar{\psi}_{\text{R}} \approx \frac{1}{i\omega\mu_0}\overline{\overline{G}}_{\text{R–TID}} \cdot \overline{\overline{P}}_{2,\text{TID}} \cdot \overline{E}_{\text{inc,TID}} + \overline{\overline{G}}_{\text{s}} \cdot \overline{\overline{E}}_{\text{inc}} \cdot \bar{\chi}. \tag{35}$$

Therefore, the cost function of the proposed SRA method is defined as

$$f(\overline{\chi}) = \sum_{p=1}^{N_i} \left\|\begin{array}{c}\overline{\overline{G}}_{\text{s}} \cdot \overline{\overline{E}}_{\text{inc}}^p \cdot \bar{\chi} - \bar{E}_{\text{inc,R}}^p \cdot \bar{\psi}_{1,\text{R}}^p \\ + \frac{1}{i\omega\mu_0}\overline{\overline{G}}_{\text{R–TID}} \cdot \overline{\overline{P}}_{2,\text{TID}}^p \cdot \overline{E}_{\text{inc,TID}}^p\end{array}\right\|^2 + \beta\|\overline{\chi}\|^2. \tag{36}$$

The minimizer of (36) is

$$\overline{\chi} = \left[\sum_{p=1}^{N_i}\left(\overline{\overline{G}}_{\text{s}} \cdot \overline{\overline{E}}_{\text{inc}}^p\right)^H \cdot \left(\overline{\overline{G}}_{\text{s}} \cdot \overline{\overline{E}}_{\text{inc}}^p\right) + \beta\overline{\overline{I}}\right]^{-1}$$
$$\cdot \left\{\sum_{p=1}^{N_i}\begin{array}{c}\left(\overline{\overline{G}}_{\text{s}} \cdot \overline{\overline{E}}_{\text{inc}}^p\right)^H \\ \cdot \left[\bar{E}_{\text{inc,R}}^p \cdot \bar{\psi}_{\text{R}}^p - \frac{1}{i\omega\mu_0}\overline{\overline{G}}_{\text{R–TID}} \cdot \overline{\overline{P}}_{2,\text{TID}}^p \cdot \overline{E}_{\text{inc,TID}}^p\right]\end{array}\right\}. \tag{37}$$

The overhead computational cost of the SRA method, compared with the RA inversion method, is the computational cost of the retained term. The computational cost of the retained term is dominated by the cost of the calculation of the scattered field within the TID generated by the major induced current. The overhead computational cost of the SRA method is $O(M_{\text{TID}}\log M_{\text{TID}} + M_{\text{DOI}}N_s^2)$, where $O(M_{\text{DOI}}N_s^2)$ is the computational cost of the thin SVD of $\overline{\overline{G}}_{\text{s}}$.

3) Joint Method: The SRA method and the MBA method are based on linear equations using different approximations to solve for contrast. The SRA is based on (35), and the MBA method [13] is based on the following equation:

$$\bar{E}_{\text{s}} \approx \overline{\overline{G}}_{\text{s}} \cdot \overline{\overline{E}}_{\text{ta}} \cdot \overline{\chi} \tag{38}$$

where

$$\overline{E}_{\text{ta}} = \overline{E}_{\text{inc}} + \overline{\overline{G}}_{\text{d}} \cdot \overline{J}^+. \tag{39}$$

Solving the equations of the MBA and SRA methods together, the cost function of the joint method is

$$f(\overline{\chi}) = \left[\sum_{p=1}^{N_i}\begin{array}{c}\left\|\begin{array}{c}\overline{\overline{G}}_{\text{s}} \cdot \overline{\overline{E}}_{\text{inc}}^p \cdot \bar{\chi} - \bar{E}_{\text{inc,R}}^p \cdot \bar{\psi}_{\text{R}}^p + \\ \frac{1}{i\omega\mu_0}\overline{\overline{G}}_{\text{R–TID}} \cdot \overline{\overline{P}}_{2,\text{TID}}^p \cdot \overline{E}_{\text{inc,TID}}^p\end{array}\right\|^2 \\ + \left\|\overline{\overline{G}}_{\text{s}} \cdot \overline{\overline{E}}_{\text{ta}}^p \cdot \overline{\chi} - \overline{E}_{\text{s}}^p\right\|^2\end{array}\right] + \beta\|\overline{\chi}\|^2. \tag{40}$$

The minimizer of (40) is

$$\overline{\chi} = \left(\sum_{p=1}^{N_i}\overline{\overline{T}}_1^p + \beta\overline{\overline{I}}\right)^{-1} \cdot \left(\sum_{p=1}^{N_i}\overline{\overline{T}}_2^p\right) \tag{41}$$
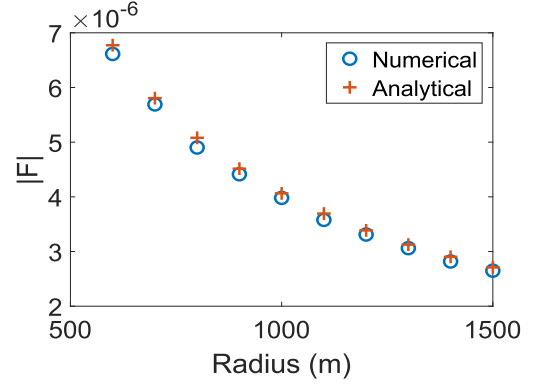
Fig. 2. Comparison between F_{anal} in (18) and F_{num} in (19).

where $\overline{\overline{T}}_1^p = (\overline{\overline{G}}_{\text{s}} \cdot \overline{\overline{E}}_{\text{inc}}^p)^H \cdot \overline{\overline{G}}_{\text{s}} \cdot \overline{\overline{E}}_{\text{inc}}^p + (\overline{\overline{G}}_{\text{s}} \cdot \overline{\overline{E}}_{\text{ta}}^p)^H \cdot \overline{\overline{G}}_{\text{s}} \cdot \overline{\overline{E}}_{\text{ta}}^p$, and $\overline{\overline{T}}_2^p = (\overline{\overline{G}}_{\text{s}} \cdot \overline{\overline{E}}_{\text{ta}}^p)^H \cdot \overline{E}_{\text{s}}^p + (\overline{\overline{G}}_{\text{s}} \cdot \overline{\overline{E}}_{\text{inc}}^p)^H \cdot (\overline{E}_{\text{inc,R}}^p \cdot \bar{\psi}_{\text{R}}^p - 1/i\omega\mu_0 \cdot \overline{\overline{G}}_{\text{R–TID}} \cdot \overline{\overline{P}}_{2,\text{TID}}^p \cdot \overline{E}_{\text{inc,TID}}^p)$.

III. NUMERICAL RESULTS

A. Comparison of F_{anal} and F_{num}

To compare F_{anal} and F_{num} with the increasing radius ρ' when $\rho' \gg \rho$, F_{anal} and F_{num} are calculated for different radii ρ' and plotted in Fig. 2.

In this section, we consider a cylinder with a relative permittivity of 1.4 and a radius of 0.2 m. The operating frequency is 400 MHz, and the incident field is a plane wave propagating in the x-direction. The observation point of (18) and (19) is at $(3 \text{ m}, 0°)$.

From Fig. 2, it could be observed that F_{anal} and F_{num} are consistent with each other. Both F_{anal} and F_{num} decrease with the increasing radius ρ', which is also suggested in (18). The consistency of F_{anal} with F_{num} in Fig. 2 has verified the formula of F_{anal} in (18). Based on (18), it is proven in Section II-C that $\int_r^\infty F_{\text{anal}}(\rho, \phi, \rho')d\rho'$ is negligible if r is large enough. Therefore, for an arbitrary scatterer, the first integral in (9) could be well approximated by an appropriate truncation of the integral domain.

B. Comparison of the Errors err_1 and $err_{1,2}$ Using Different Sizes of the TID

To investigate how the errors err_1 and $err_{1,2}$, which are defined in (26) and (31), respectively, will vary with the increasing side length of the TID, the errors are plotted in this section.

We consider a cylinder with a relative permittivity of 1.7 and a radius of 0.4 m illuminated by 16 plane-wave incidences from different directions of 400 MHz. The major induced current is calculated using $L = 15$. The size of the DOI is 2 m × 2 m. The errors err_1 and $err_{1,2}$ are plotted in Fig. 3. Note the horizontal axis corresponds to the side length of the TID, which is a square. From Fig. 3, there are mainly two observations as follows. First, using complete induced current, err_1 will decrease with increasing side length of TID, and err_1 is negligible when the side length is large enough. Second, using major induced current, $err_{1,2}$ will decrease until a threshold value of side length, which is equal to triple side
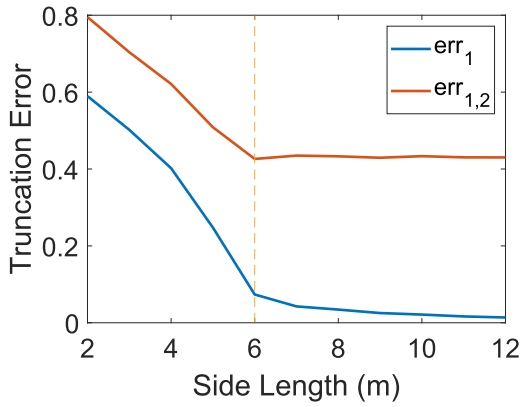
Fig. 3. Truncation errors defined in (26) and (31) using different sizes of TID.

TABLE II
RELATIVE ERRORS OF DIFFERENT METHODS

	BA	RA	MBA	SRA	Joint
Austria	12.96%	11.85%	9.64%	8.23%	7.66%
Alphabet	12.78%	12.26%	11.36%	9.59%	9.36%
Large Square ($\varepsilon_r = 1.4$)	14.81%	10.62%	13.41%	8.67%	7.01%
Small Square ($\varepsilon_r = 2.3$)	25.72%	25.45%	17.03%	21.57%	18.86%
Experiment	37.11%	37.03%	27.49%	30.99%	27.62%

TABLE III
INVERSION TIME OF DIFFERENT METHODS

	BA	RA	MBA	SRA	Joint
Time (s)	0.89	0.91	1.03	1.49	1.77

length of the DOI in this case, is reached. Beyond the threshold value of the side length, blindly increasing the side length of the TID does not generate a lower value of $err_{1,2}$, and it will increase the computational cost of the inversion method.

From simulations with many mild scatterers of various shapes, we observed a common feature in the variation of truncation error with the size of TID; i.e., although the truncation error decreases as the TID size increases, a point will always be reached at several times of the DOI size; after that point, further enlargement of the TID size yields diminishing and negligible reduction of truncation error, as illustrated in Fig. 3. This phenomenon indicates that the major contribution to the integral in (14) is attributed to a scatterers-centered domain several times as large as DOI. Choosing an appropriate value of the side length of TID is helpful to obtain better reconstructions at relatively low computational cost in the inverse problem.

C. Tests With Austria Profile

In the Sections III-C–III-G, both the DOI and the TID are squares. In the Sections III-C–III-E, the size of the DOI is 2 m × 2 m, and the size of the TID is 6 m × 6 m. The size of the TID is determined empirically, since no prior information is available. It is noteworthy that it is not always necessary to accurately determine the size of TID for two reasons. First, as a non-iterative method, the SRA is mainly used to reconstruct scatterers that are not too strong, for which the major contribution to the integral in (14) is attributed to the scatterers-centered domain that is not very large. Second, we found in our experiments that, for mild scatterers, as long as the size of TID is larger than DOI, the SRA produces better results, compared with RA. Considering the abovementioned two points, it suffices to determine the size of TID empirically for a good balance between accuracy and computational cost. The DOI and the TID are discretized into 64 × 64 pixels and 192 × 192 pixels, respectively. The wavelength of 16 plane-wave incidences from different directions is 0.75 m. The 32 receiving antennas are uniformly placed on a circle with a radius of 3 m. The noise level of the scattered field is defined as $\|\overline{\overline{n}}\|_F / \|\overline{\overline{E}}_s\|_F$, where $\overline{\overline{n}}$ is the additive white Gaussian noise, and $\overline{\overline{E}}_s$ is the scattered field. The sizes of both $\overline{\overline{E}}_s$ and $\overline{\overline{n}}$ are $N_s \times N_i$. In this article, 5% and 15% noise levels are used,

which correspond to the SNR values of 26.02 and 16.48 dB, respectively. To evaluate the qualities of reconstructions, the relative error is defined as $\|\overline{\varepsilon}_{r,rec} - \overline{\varepsilon}_{r,exact}\| / \|\overline{\varepsilon}_{r,exact}\|$, where $\overline{\varepsilon}_{r,rec}$ is the reconstructed relative permittivity, and $\overline{\varepsilon}_{r,exact}$ is the exact relative permittivity.

In this section, the Austria profile with a relative permittivity equal to 1.4 is used. The noise level is 5%, and the value of L is, hence, determined to be 19. For the SRA method, the inversions are performed using the TIDs of sizes 2 m × 2 m and 6 m × 6 m. Benefitting from using the subspace method, it is observed from Fig. 4 that the MBA and SRA methods provide better reconstructions than the BA and RA inversion methods. Fig. 4(e) shows the improvement of the SRA method over the RA inversion method even using the TID of the same size as the DOI. The quality of the reconstruction is further improved using the SRA method with the TID of size 6 m × 6 m. The joint method, which combines the SRA and MBA methods, has a better performance than either of the SRA or MBA methods. As shown in Table II, the relative errors using BA, RA, MBA, and SRA with the TID of size 6 m × 6 m and joint methods are 12.96%, 11.85%, 9.64%, 8.23%, and 7.66%, respectively. The relative error using SRA with the TID of size 2 m × 2 m is 8.69%. The inversion time using different methods is shown in Table III. Note that the time for determination of regularization coefficients is not included, which is usually less than 1 s.

D. Tests With Alphabetic Profile

In this section, an alphabetic profile is used, as displayed in Fig. 5(a). The relative permittivity of the scatterer is 1.5. The noise level is 15%, and L is determined to be 16. From Fig. 5(b) and (c), the reconstructed relative permittivity using the BA and RA inversion methods is much less than the exact permittivity of the scatterer, and prominent artifacts exist in the reconstructions. In comparison, the reconstructed permittivity of the MBA, SRA, and joint methods in Fig. 5(d)–(f) is closer to the exact value, and the artifacts are less prominent. The relative errors of the reconstructions using the BA and RA
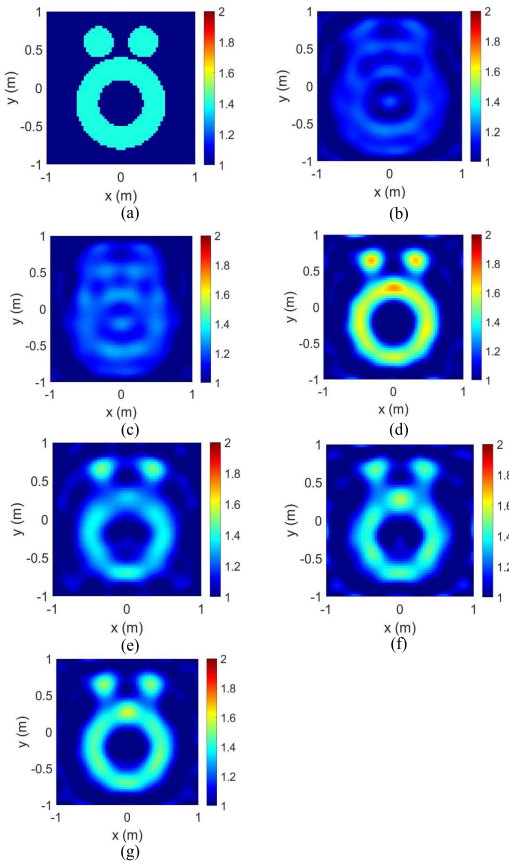
Fig. 4. (a) Austria profile with a relative permittivity equal to 1.4, and reconstructions with 5% noise using (b) BA inversion method, (c) RA inversion method, (d) MBA method, (e) SRA method (TID: 2 m × 2 m, the same as the DOI), (f) SRA method (TID: 6 m × 6 m), and (g) joint method.

inversion methods are 12.78% and 12.26%, respectively. Also, the relative errors using the MBA, SRA, and joint methods are 11.36%, 9.59%, and 9.36%, respectively.

E. Test With Large Square Profile

In this section, the side length of the square is 1.2 m. The relative permittivity of the square is 1.4. The noise level is 5%, and L is 19. Since the electrical size of this scatterer is relatively large, it can be seen in Fig. 6 that the RA inversion method has a better performance than the BA inversion method. The relative errors of the reconstructions using the BA and RA inversion methods are 14.81% and 10.62%, respectively. Likewise, the SRA method also has a better performance than the MBA method. The relative errors of reconstructions using the MBA and SRA methods are 13.41% and 8.67%, respectively. The relative error of the reconstructed profile using the joint method is 7.01%.

F. Test With Small Square Profile

In this section, the size of the DOI is 1 m × 1 m, and the size of the TID is 3 m × 3 m. The incidences and the measurement setup are the same as in Sections II-C–II-E. The side length of the square scatterer is 0.3 m, and the relative permittivity is 2.3. The noise level is 5%, and L is 11. Unlike the example in Section III-E, it could be seen from Fig. 7 that
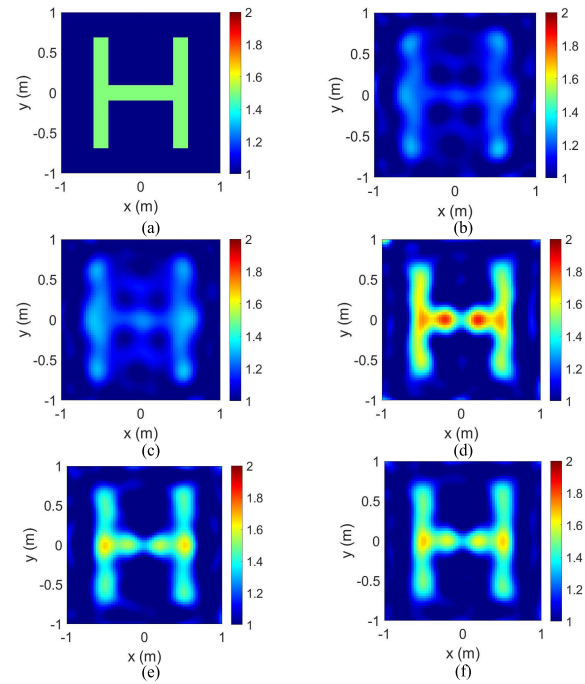

Fig. 5. (a) Alphabetic profile with a relative permittivity equal to 1.5, and reconstructions with 15% noise using (b) BA inversion method, (c) RA inversion method, (d) MBA method, (e) SRA method, and (f) joint method.
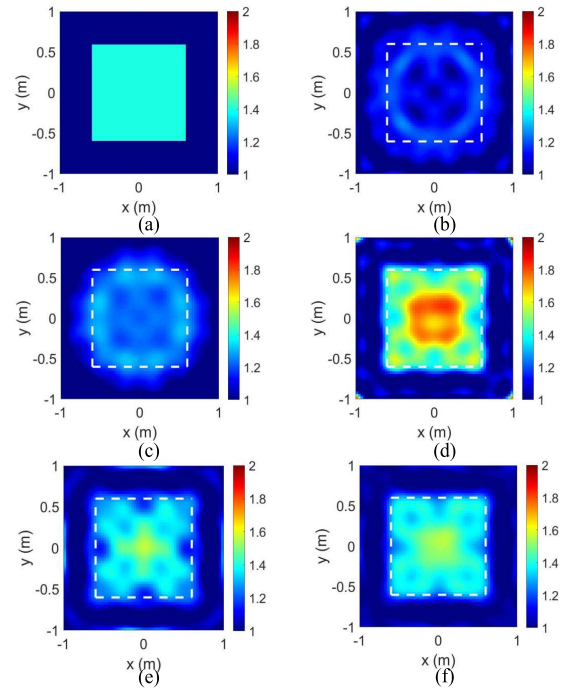

Fig. 6. (a) Large square profile with a relative permittivity equal to 1.4, and reconstructions with 5% noise using (b) BA inversion method, (c) RA inversion method, (d) MBA method, (e) SRA method, and (f) joint method.

the reconstructed permittivity using the MBA method is closer to the exact permittivity than the SRA method. The MBA, SRA, and joint methods all outperform the BA and RA inversion methods. The relative errors using the BA and RA methods are 25.72% and 25.45%, respectively. The relative errors using the MBA, SRA, and joint methods are 17.03%, 21.57%, and 18.86%, respectively.
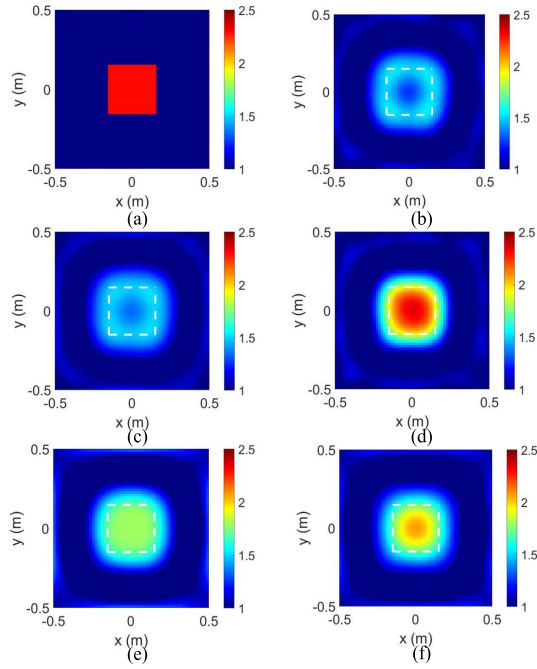
Fig. 7. (a) Small square profile with a relative permittivity equal to 2.3, and reconstructions with 5% noise using (b) BA inversion method, (c) RA inversion method, (d) MBA method, (e) SRA method, and (f) joint method.
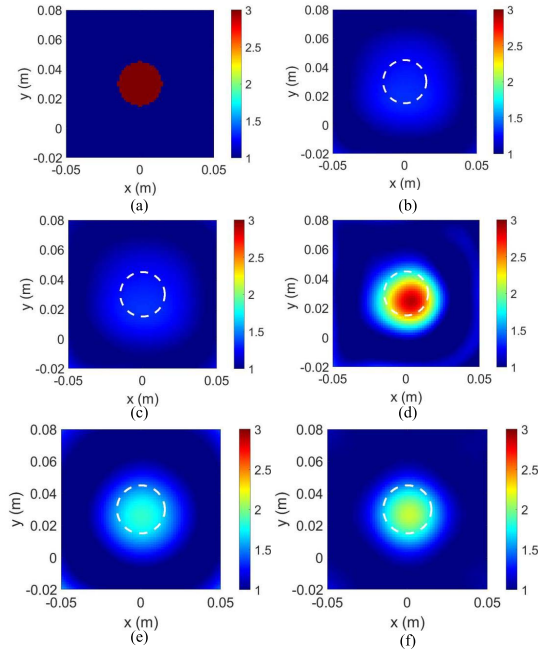

Fig. 8. (a) Experimental profile, and reconstructions using (b) BA inversion method, (c) RA inversion method, (d) MBA method, (e) SRA method, and (f) joint method.

G. Test With Experimental Data

In this section, the proposed methods are validated using experimental data.

In the experiment [27], the wavelength of the incidences is 0.1 m. The sizes of the DOI and the TID are 0.1 m × 0.1 m and 0.3 m × 0.3 m, respectively. The DOI is discretized into 64 × 64 pixels, and the TID is discretized into 192 × 192 pixels. The transmitting antenna is revolved along the circle

with the radius of 0.72 ± 0.003 m around the object at the step size of $10°$. The receiving antenna is revolved along the circle with the radius of $0.76 \pm 0.d003$ m around the object at the step size of $5°$. The smallest angular distance between the transmitting antenna and the receiving antenna is $60°$. Due to the absence of the prior information about the measurement noise level, the value of L is chosen, such that the corresponding singular value is about 50% of the maximum singular value [28], which is equal to 5 in this example. The relative permittivity of the cylindrical scatterer is 3 ± 0.3, and the radius is 0.015 m. The dimension of the scatterer is small, and the contrast of the scatterer is relatively high. For such kind of scatterers, it could be seen from Fig. 8 that the RA inversion method has almost no advantage over the BA inversion method. The relative errors of the BA and the RA inversion methods are 37.11% and 37.03%, respectively. The MBA method has a better performance than the SRA method. The relative errors of the MBA, SRA, and joint methods are 27.49%, 30.99%, and 27.62%, respectively.

The results are similar to those in Section III-F. For both examples, where the scatterers are relatively small and the contrasts are relatively large, the MBA method outperforms the proposed SRA method.

IV. CONCLUSION AND DISCUSSION

In this article, we have proposed a method to evaluate the neglected term in RA so as to improve inversion results. Our method consists of two approximations, where the integrand is quantified by the subspace method, and the integral is performed on a finite domain instead of the whole space.

The contributions of the proposed method are threefold. First, the SRA method outperforms the RA and BA inversion methods in reconstructing relatively strong scatterers, by retaining the term neglected by RA and incurring a small additional computational cost of $O(M_{\text{TID}}\log M_{\text{TID}} + M_{\text{DOI}} N_s^2)$. Second, for reconstructions of scatterers with relatively large electrical sizes, the SRA method outperforms the MBA method, just as RA outperforms BA. Third, inversion results may further be improved by combining the SRA method with other non-iterative inversion methods, such as the joint method proposed in this article, which is a combination of the SRA method and the MBA method.

APPENDIX

We derive the analytical formula of $F(\rho, \phi, \rho')$ for large ρ' in this section.

Assume that the incident field is propagating in the positive x-axis, the incident field is expanded as

$$E_{\text{inc}}(\rho', \phi') = e^{ikx'} = \sum_n i^n J_n(k\rho') e^{in\phi'}. \quad (A1)$$

It is known that

$$\exp(-ir\cos\phi) = \sum_n (-i)^n J_n(r) e^{in\phi} \quad (A2)$$

$$\lim_{x\to\infty} H_m^{(1)}(x) = \sqrt{\frac{2}{\pi x}} \exp\left[i\left(x - \frac{m\pi}{2} - \frac{\pi}{4}\right)\right] \quad (A3)$$

$$\lim_{x\to\infty} J_m(x) = \sqrt{\frac{2}{\pi x}} \cos\left[i\left(x - \frac{m\pi}{2} - \frac{\pi}{4}\right)\right]. \quad (A4)$$

Assuming ρ' is large enough, the scattered field is expanded as

$$
\begin{aligned}
E_s(\rho', \phi') &= -\frac{\omega \mu_0}{4} \sum_n b_n H_n^{(1)}(k\rho') e^{in\phi'} \\
&= \sqrt{\frac{1}{\rho'}} \exp(ik\rho') \sum_n -\frac{\omega \mu_0}{4} b_n \sqrt{\frac{2}{\pi k}} \\
&\quad \times \exp\left[i\left(-\frac{n\pi}{2} - \frac{\pi}{4} + n\phi' \right) \right].
\end{aligned} \tag{A5}
$$

Consequently

$$
\nabla' E_s(\rho', \phi') \approx ik E_s(\rho', \phi') \hat{\rho}' \tag{A6}
$$

$$
\begin{aligned}
\nabla' \psi_1(\rho', \phi') &= \nabla' \left[\ln \frac{E_s(\rho', \phi') + E_{\text{inc}}(\rho', \phi')}{E_{\text{inc}}(\rho', \phi')} \right] \\
&\approx \nabla' \frac{E_s(\rho', \phi')}{E_{\text{inc}}(\rho', \phi')}
\end{aligned} \tag{A7}
$$

$$
\begin{aligned}
\left(\nabla' \psi_1 \right)^2 &= \left(\nabla' \psi_1 \right) \cdot \left(\nabla' \psi_1 \right) \\
&\approx -2k^2 \left(\frac{E_s}{E_{\text{inc}}} \right)^2 + 2k^2 \cos\phi' \left(\frac{E_s}{E_{\text{inc}}} \right)^2.
\end{aligned} \tag{A8}
$$

According to addition theorem, for $\rho < \rho'$

$$
H_0^{(1)}(kR) = \sum_n H_n^{(1)}(k\rho') J_n(k\rho) \cos\left[n(\phi - \phi') \right] \tag{A9}
$$

where $R = \sqrt{\rho^2 + \rho'^2 - 2\rho\rho' \cos(\phi - \phi')}$.

By substituting (A1), (A5), (A8), and (A9) into (15), it is obtained that

$$
\begin{aligned}
F(\rho') &= \int_0^{2\pi} \frac{i}{4} H_0^{(1)}(kR) \left(\nabla' \psi_1 \right)^2 E_{\text{inc}} \rho' d\phi' \\
&\approx \int_0^{2\pi} \frac{i}{4} \sum_n H_n^{(1)}(k\rho') J_n(k\rho) \cos\left(n(\phi - \phi') \right) \\
&\quad \times 2k^2 \left(-1 + \cos\phi' \right) E_s^2 E_{\text{inc}}^* \rho' d\phi' \\
&\approx \sum_m \sum_n \sum_p \sum_q
\begin{bmatrix}
i J_n(k\rho) k \dfrac{\omega^2 \mu_0^2}{16} \dfrac{b_q b_p}{\pi} \\
\times \exp\left(-i \dfrac{p+q+1}{2} \pi \right) (-i)^m \\
\int_0^{2\pi} \dfrac{1}{4} f_1(n, t_1 + 1, t_2 + 1, \phi, \phi') \\
+ \dfrac{1}{4} f_1(n, t_1 - 1, t_2 - 1, \phi, \phi') \\
- \dfrac{1}{2} f_1(n, t_1, t_2, \phi, \phi') d\phi' \\
H_n^{(1)}(k\rho') \exp(i2k\rho') J_m(k\rho')
\end{bmatrix}
\end{aligned} \tag{A10}
$$

where $t_1 = p + q + m - n$, $t_2 = p + q + m + n$, $f_1(n, u, v, \phi, \phi') = \exp(in\phi + iu\phi') + \exp(-in\phi + iv\phi')$.

After elimination of n, (A10) becomes

$$
\begin{aligned}
F(\rho') &\approx \frac{i}{8} k\omega^2 \mu_0^2 \exp(i2k\rho') \\
&\quad \times \sum_m \sum_p \sum_q \Bigg[\frac{1}{4} f_2(t_3 + 1, \rho, \phi, \rho') \\
&\qquad\qquad + \frac{1}{4} f_2(t_3 - 1, \rho, \phi, \rho') \\
&\qquad\qquad - \frac{1}{2} f_2(t_3, \rho, \phi, \rho') \Bigg] (-i)^m J_m(k\rho') b_q b_p \\
&\quad \times \exp\left(-i \frac{p+q+1}{2} \pi \right)
\end{aligned} \tag{A11}
$$

where $t_3 = m + p + q$, $f_2(t, \rho, \phi, \rho') = J_t(k\rho) \exp(it\phi) H_t^{(1)}(k\rho') + J_{-t}(k\rho) \exp(it\phi) H_{-t}^{(1)}(k\rho')$.

By substituting (A3) and (A4) into (A11), it is obtained that

$$
\begin{aligned}
F(\rho') &\approx i \frac{\omega^2 \mu_0^2}{8\pi \rho'} \exp\left(-i\left(-2k\rho' + \frac{\pi}{2} \right) \right) \\
&\quad \times \sum_m \sum_p \sum_q \Bigg[\frac{1}{4} f_3(t_3 + 1, \rho, \phi, \rho') + \frac{1}{4} f_3(t_3 - 1, \rho, \phi, \rho') \\
&\qquad\qquad - \frac{1}{2} f_3(t_3, \rho, \phi, \rho') \Bigg] b_p b_q \exp\left(-i \frac{p+q}{2} \pi \right)
\end{aligned} \tag{A12}
$$

where $f_3(t, \rho, \phi, \rho') = (-i)^t J_t(k\rho) \exp[it(\phi - \pi)] \exp\{i[2k\rho' + (p + q + t - t_3)\pi - \pi/2]\} + (-i)^t J_t(k\rho) \exp(it\phi) + (-i)^t J_{-t}(k\rho) \exp[it(\phi + \pi)] + (-i)^t J_{-t}(k\rho) \exp(it\phi) \exp\{i[2k\rho' + (p + q + t - t_3)\pi - \pi/2]\}$.

By substituting (A2) into (A12), it is obtained that

$$
F(\rho') \approx \exp(i4k\rho') i \frac{\omega^2 \mu_0^2}{4\pi \rho'} \exp(ik\rho \cos\phi) \sum_p \sum_q b_p b_q i^{p+q}. \tag{A13}
$$

REFERENCES

[1] X. Chen, *Computational Methods for Electromagnetic Inverse Scattering*. Singapore: Wiley, 2018.

[2] P. M. van den Berg, A. L. Van Broekhoven, and A. Abubakar, "Extended contrast source inversion," *Inverse Problems*, vol. 15, no. 5, pp. 1325–1344, Aug. 1999.

[3] W. C. Chew and Y. M. Wang, "Reconstruction of two-dimensional permittivity distribution using the distorted Born iterative method," *IEEE Trans. Med. Imag.*, vol. 9, no. 2, pp. 218–225, Jun. 1990.

[4] T. Isernia, L. Crocco, and M. D'Urso, "New tools and series for forward and inverse scattering problems in lossy media," *IEEE Geosci. Remote Sens. Lett.*, vol. 1, no. 4, pp. 327–331, Oct. 2004.

[5] X. Chen, "Subspace-based optimization method for solving inverse-scattering problems," *IEEE Trans. Geosci. Remote Sens.*, vol. 48, no. 1, pp. 42–49, Aug. 2010.

[6] Y. Zhong, M. Lambert, D. Lesselier, and X. Chen, "A new integral equation method to solve highly nonlinear inverse scattering problems," *IEEE Trans. Antennas Propag.*, vol. 64, no. 5, pp. 1788–1799, May 2016.

[7] M. Slaney, A. C. Kak, and L. E. Larsen, "Limitations of imaging with first-order diffraction tomography," *IEEE Trans. Microw. Theory Techn.*, vol. MTT-32, no. 8, pp. 860–874, Aug. 1984.

[8] T. M. Habashy, R. W. Groom, and B. R. Spies, "Beyond the Born and Rytov approximations: A nonlinear approach to electromagnetic scattering," *J. Geophys. Res., Solid Earth*, vol. 98, no. B2, pp. 1759–1775, Feb. 1993.

[9] A. J. Devaney, "Inverse-scattering theory within the Rytov approximation," *Opt. Lett.*, vol. 6, no. 8, pp. 374–376, Aug. 1981.

[10] L. Crocco, I. Catapano, L. D. Donato, and T. Isernia, "The linear sampling method as a way to quantitative inverse scattering," *IEEE Trans. Antennas Propag.*, vol. 60, no. 4, pp. 1844–1853, Apr. 2012.

[11] L. D. Donato and L. Crocco, "Model-based quantitative cross-borehole GPR imaging via virtual experiments," *IEEE Trans. Geosci. Remote Sens.*, vol. 53, no. 8, pp. 4178–4185, Aug. 2015.

[12] M. T. Bevacqua, L. Crocco, L. Di Donato, and T. Isernia, "An algebraic solution method for nonlinear inverse scattering," *IEEE Trans. Antennas Propag.*, vol. 63, no. 2, pp. 601–610, Feb. 2015.

[13] T. Yin, Z. Wei, and X. Chen, "Non-iterative methods based on singular value decomposition for inverse scattering problems," *IEEE Trans. Antennas Propag.*, vol. 68, no. 6, pp. 4764–4773, Jun. 2020.

[14] J. B. Keller, "Accuracy and validity of the Born and Rytov approximations," *J. Opt. Soc. Amer. A, Opt. Image Sci.*, vol. 59, no. 8, pp. 1003–1004, Jul. 1969.

[15] A. Dubey, P. Sood, J. Santos, D. Ma, C.-Y. Chiu, and R. Murch, "An enhanced approach to imaging the indoor environment using WiFi RSSI measurements," *IEEE Trans. Veh. Technol.*, vol. 70, no. 9, pp. 8415–8430, Sep. 2021.

[16] D. Tajik, N. K. Nikolova, and M. D. Noseworthy, "Improving quantitative microwave holography through simultaneous use of the Born and Rytov approximations," in *Proc. 16th Eur. Radar Conf. (EuRAD)*, 2019, pp. 281–284.

[17] S. Caorsi, A. Massa, and M. Pastorino, "Rytov approximation: Application to scattering by two-dimensional weakly nonlinear dielectrics," *J. Opt. Soc. Amer. A, Opt. Image Sci.*, vol. 13, no. 3, pp. 509–516, Mar. 1996.

[18] L. Manica, P. Rocca, M. Salucci, M. Carlin, and A. Massa, "Scattering data inversion through interval analysis under Rytov approximation," in *Proc. 7th Eur. Conf. Antennas Propag. (EuCAP)*, 2013, pp. 82–85.

[19] G. Oliveri, L. Poli, P. Rocca, and A. Massa, "Bayesian compressive optical imaging within the Rytov approximation," *Opt. Lett.*, vol. 37, no. 10, pp. 1760–1762, May 2012.

[20] L. Li, W. Zhang, and F. Li, "Tomographic reconstruction using the distorted Rytov iterative method with phaseless data," *IEEE Geosci. Remote Sens. Lett.*, vol. 5, no. 3, pp. 479–483, Jul. 2008.

[21] X. Ye and X. Chen, "Subspace-based distorted-born iterative method for solving inverse scattering problems," *IEEE Trans. Antennas Propag.*, vol. 65, no. 12, pp. 7224–7232, Dec. 2017.

[22] J. A. Kong, *Electromagnetic Wave Theory*. New York, NY, USA: Wiley, 1990.

[23] M. Abramowitz and I. A. Stegun, *Handbook of Mathematical Functions: With Formulas, Graphs, and Mathematical Tables*. New York, NY, USA: Dover, 1965.

[24] A. Kirsch, *An Introduction to the Mathematical Theory of Inverse Problems*. Berlin, Germany: Springer, 2011.

[25] M. Belge, M. E. Kilmer, and E. L. Miller, "Efficient determination of multiple regularization parameters in a generalized L-curve framework," *Inverse Problems*, vol. 18, no. 4, pp. 1161–1183, Jul. 2002.

[26] P. C. Hansen, "Regularization tools: A MATLAB package for analysis and solution of discrete ill-posed problems," *Numer. Algorithms*, vol. 6, no. 1, pp. 1–35, Oct. 1994.

[27] K. Belkebir and M. Saillard, "Testing inversion algorithms against experimental data," *Inverse Problems*, vol. 17, no. 6, pp. 1565–1571, Nov. 2001.

[28] Z. Wei and X. Chen, "Deep-learning schemes for full-wave nonlinear inverse scattering problems," *IEEE Trans. Geosci. Remote Sens.*, vol. 57, no. 4, pp. 1849–1860, Apr. 2018.

Tiantian Yin received the B.E. degree (Hons.) in electrical and electronic engineering from Nanyang Technological University, Singapore, in 2016, and the Ph.D. degree in electrical and computer engineering from the National University of Singapore, Singapore, in 2021.

She is currently a Research Fellow with the National University of Singapore. Her research interest includes electromagnetic inverse scattering problems.

Dr. Yin was a recipient of the 2020 Best Student Paper Competition Award from the IEEE Singapore Microwave Theory and Techniques/Antennas and Propagation (MTT/AP) Chapter.

Li Pan (Member, IEEE) received the B.Sc. degree in electrical and computer engineering (ECE) from Zhejiang University, Hangzhou, China, in 2003, the M.Sc. degree in ECE from the Chalmers University of Technology, Gothenburg, Sweden, in 2006, and the Ph.D. degree in ECE from the National University of Singapore, Singapore, in 2011.

He was with the Department of Sensor Physics, Halliburton, Singapore, from 2012 to 2022, where he developed various electromagnetic (EM) forward modeling and inversion algorithms for the novel EM-based downhole formation evaluation services for oil and gas reservoir detection. He joined Huawei, Singapore, in 2022, as an Expert in EM sensing, and his work involves the research and development in the area of integrated sensing and communication (ISAC) for 6G. His research interest includes numerical methods for EM modeling and inverse problems.

Xudong Chen (Fellow, IEEE) received the B.S. and M.S. degrees from Zhejiang University, Hangzhou, China, in 1999 and 2001, respectively, and the Ph.D. degree from the Massachusetts Institute of Technology, Cambridge, MA, USA, in 2005.

Since 2005, he has been with the National University of Singapore, Singapore, where he is currently a Professor. He has authored or coauthored 160 journal papers on inverse scattering problems, material parameter retrieval, microscopy, and optical encryption. He has authored the book *Computational Methods for Electromagnetic Inverse Scattering* (Wiley-IEEE, 2018). His research interests include mainly electromagnetic wave theories and applications, with a focus on inverse problems and computational imaging. He is recently working on mm-wave imaging algorithms and solving inverse problems via machine learning.

Dr. Chen is a fellow of the Electromagnetics Academy. He has been the members of organizing committees of more than ten conferences. He was a recipient of the Young Scientist Award by the Union Radio Scientifique Internationale in 2010 and the Ulrich L. Rohde Innovative Conference Paper Award at the IEEE International Conference on Computational Electromagnetics (ICCEM) in 2019. He was the Chair of the IEEE Singapore Microwave Theory and Techniques/Antennas and Propagation (MTT/AP) Joint Chapter in 2018. He has been serving as the General Chair, the Technical Program Committee (TPC) Chair, and the Award Committee Chair. He was an Associate Editor of the IEEE TRANSACTIONS ON MICROWAVE THEORY AND TECHNIQUES from 2015 to 2019. He is currently an Associate Editor of the IEEE TRANSACTIONS ON GEOSCIENCE AND REMOTE SENSING and the IEEE JOURNAL OF ELECTROMAGNETICS, RF AND MICROWAVE IN MEDICINE AND BIOLOGY.